Nuclear Materials and Energy 34 (2023) 101308

Contents lists available at ScienceDirect

Nuclear Materials and Energy

journal homepage: www.elsevier.com/locate/nme

Prospects of core–edge integrated no-ELM and small-ELM scenarios for future fusion devices

E. Viezzer [a,*], M.E. Austin [b], M. Bernert [c], K.H. Burrell [d], P. Cano-Megias [e], X. Chen [d], D.J. Cruz-Zabala [a], S. Coda [f], M. Faitsch [c], O. Février [f], L. Gil [g], C. Giroud [h], T. Happel [c], G.F. Harrer [i], A.E. Hubbard [j], J.W. Hughes [j], A. Kallenbach [c], B. Labit [f], A. Merle [f], H. Meyer [h], C. Paz-Soldan [k], P. Oyola [a], O. Sauter [f], M. Siccinio [l], D. Silvagni [c], E.R. Solano [m], EUROfusion WPTE and ASDEX Upgrade Teams

[a] Department of Atomic, Molecular and Nuclear Physics, University of Seville, Av. Reina Mercedes, Seville, 41012, Spain
[b] The University of Texas at Austin, Austin, 78712, Texas, USA
[c] Max Planck Institute for Plasma Physics, Boltzmannstr. 2, Garching, 85748, Germany
[d] General Atomics, P.O. Box 85608, San Diego, 92186-5608, CA, United States
[e] Department of Energy Engineering, University of Seville, Camino de los Descubrimientos s/n, Isla de la Cartuja, Seville, 41092, Spain
[f] Ecole Polytechnique Federale de Lausanne (EPFL), Swiss Plasma Center (SPC), Lausanne, 1015, Switzerland
[g] Instituto de Plasmas e Fusao Nuclear, Instituto Superior Tecnico, Universidade de Lisboa, Lisboa, 1049-001, Portugal
[h] Culham Center for Fusion Energy, Culham Science Centre, Abingdon, United Kingdom
[i] Institute of Applied Physics, TU Wien, Wiedner Hauptstr. 8-10, Vienna, 1040, Austria
[j] MIT Plasma Science and Fusion Center, Cambridge MA, United States of America
[k] Department of Applied Physics and Applied Mathematics, Columbia University, New York, 10027, United States of America
[l] EUROfusion Consortium, Garching, 85748, Germany
[m] Laboratorio Nacional de Fusion, CIEMAT, Madrid, Spain

ARTICLE INFO

MSC:
00A79

Keywords:
Plasma confinement and transport
Edge localized modes
Core–edge integration

ABSTRACT

One of our grand challenges towards fusion energy is the achievement of a high-performance plasma core coupled to a boundary solution. The high confinement mode (H-mode) provides such a high-performance fusion core due to the build-up of an edge transport barrier leading to a pedestal. However, it usually features type-I edge localized modes (ELMs) which pose a threat for long-duration plasma operation in future fusion devices as they induce large energy fluences onto the plasma facing components and typically are projected to damage the first wall.

For future fusion devices, the integration of a stationary no-ELM regime with a power exhaust solution is indispensable. Several no-ELM and small-ELM regimes have extended their operational space in the past years, with the ultimate goal of providing an alternative core–edge solution to ITER and EU-DEMO. Prominent no-ELM or small-ELM alternatives include the I-mode, QH-mode, EDA H-mode, quasi-continuous exhaust (QCE) and 'grassy' ELM regimes, X-point radiator scenarios and negative triangularity L-mode. The state-of-the-art, including access conditions and main signatures, of these alternative regimes is reviewed. Many of these regimes partly match the operational space of ITER and EU-DEMO, however, knowledge gaps remain. Besides compatibility with divertor detachment and a radiative mantle, these include extrapolations to high Q operations, low core collisionality, high Greenwald fractions, impurity transport, amongst others. The knowledge gaps and possible strategies to close these gaps to show their applicability to ITER and EU-DEMO are discussed.

1. Introduction

A key scientific issue in the quest for fusion power is improving and maintaining plasma performance on a steady-state and economical basis. At present, the highest attainable pressure is achieved in the high-confinement regime (H-mode) [1]. The H-mode is accompanied by a sharp decrease in the edge fluctuation level, the formation of an edge transport barrier and the build-up of a steep edge pressure gradient

* Corresponding author.
E-mail address: eviezzer@us.es (E. Viezzer).

https://doi.org/10.1016/j.nme.2022.101308
Received 7 August 2022; Received in revised form 7 November 2022; Accepted 15 November 2022
Available online 22 November 2022

(pedestal). The plasma confinement in the core is directly connected to the pedestal since its height sets the boundary condition for the core plasma performance. However, the pedestal pressure is limited by the occurrence of Edge Localized Modes (ELMs) [2,3], magnetohydrodynamic (MHD) instabilities that cause a transient collapse of the pedestal and the good confinement. When they exceed the MHD stability limit, the explosive ELM ejects energy and particles onto open field lines and plasma facing components [4], causing erosion and energy loads onto divertor target plates [5], at levels unacceptable in future burning plasma devices [6].

Based on the scaling of the ELM energy fluence, derived from experimental data from ASDEX Upgrade (AUG), JET and MAST, the predicted value for ITER is found to be of concern when compared to current material limits [7]. Thus, active mitigation of ELMs is planned on ITER. When extrapolating to EU-DEMO [8,9], the comparison of the predicted ELM energy fluence to current material limits becomes even more devastating [9,10], thus shifting priorities to consider no-ELM or small-ELM high-confinement alternatives for EU-DEMO [11]. This has also led the international fusion programme to dedicate substantial experimental time to the development of no-ELM and small-ELM regimes, their physics exploitation and extrapolation to ITER and DEMO-like devices.

Several "natural" no-ELM and small-ELM regimes as well as active ELM control techniques are currently being developed across all machines to ensure high confinement without the transient degradation of the pedestal caused by ELMs. To qualify the regime for EU-DEMO, the scenario needs to be robust and controllable, reproducible and compatible with EU-DEMO boundary conditions. Thus, extrapolation to future fusion devices requires not only a no-ELM solution, but also high performance and compatibility with low core and pedestal collisionality, high density and high Greenwald fraction, dominant electron heating, low torque, a metal wall, a power exhaust solution and steady state operation of the divertor.

Divertor detachment [12–14] is necessary in future fusion devices to control the surface heat flux and ensure compatibility with material surfaces [15]. The integration of a high performance burning plasma core coupled to a boundary solution remains one of our key challenges. The main reason is that a dissipative divertor is typically achieved by increasing either the electron density and/or the impurity density, often leading to a degradation of the pedestal, thus penalizing the plasma core confinement [14]. The exhaust needs for future fusion devices are further evidenced when considering the power going through the separatrix P_{sep}. For ITER, $P_{sep} = 89$ MW is expected, while for EU-DEMO $P_{sep} = 170.4$ MW [9,10]. This corresponds to $P_{sep}/R = 14.4$ MW for ITER and 18.9 MW for EU-DEMO [9,10], R being the major radius. The radiated power fraction in the core is expected to be 0.33 for ITER [15] and 0.63 for EU-DEMO [9,10].

In this paper, several "natural" no-ELM and small-ELM regimes are discussed in view of their applicability to future fusion devices. The reader is also referred to several review papers that introduce the history of many of these no-ELM/small-ELM solutions [16–21]. Note that here we will focus on the latest developments in the past five years. The operational space of many of these regimes has considerably been extended recently, with the ultimate goal of providing an alternative core–edge solution to ITER and future fusion devices. The state-of-the-art, including access conditions, main signatures and main knowledge gaps, are discussed. It should be noted that here the main focus is given to the ELM issue, while other challenges (such as the scrape-off layer power fall-off length, λ_q, scaling [22]) in view of core–edge integrated scenarios still persist and need to be tackled to ensure the integrity of future fusion devices.

This paper is organized as follows: Section 2 discusses the main actuators that allow us to achieve a "natural" no-ELM or small-ELM regime. In Section 3, the latest developments towards achieving a core–edge integrated scenario in the improved energy confinement mode (I-mode) [23–25], quiescent H-mode (QH-mode) [26,27], enhanced D_α (EDA) H-mode [28,29], type-II ELMs [30,31] (now also called Quasi-Continuous Exhaust (QCE) regime [32,33]), seeded no-ELM regimes [34] including the X-point radiator (XPR) regime [35] and negative triangularity (NT) L-modes [36,37], are presented and knowledge gaps are discussed. Section 4 maps out the experimental parameter space of these regimes and discusses strategies to close these gaps. Section 5 gives a summary of this paper.

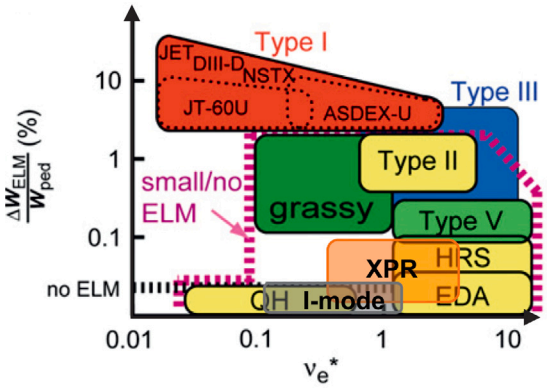

Fig. 1. Normalized ELM energy loss versus electron pedestal collisionality for a variety of scenarios, including type-I ELMy H-modes, no-ELM and small-ELM regimes. *Source:* Adapted from [17].

2. Strategies for ELM control

Over the past two decades, the development of ELM control techniques has undergone substantial progress [16]. Some require *active* control while others can be regarded as *passive* control (or "naturally" occurring). Active control techniques include ELM mitigation/suppression via magnetic perturbation coils [38–40], ELM pacing via pellets [41–43] or vertical kicks [44], localized heating and current drive at the plasma edge [45,46] or impurity seeding [47].

Besides these active control techniques, other actuators that enable the achievement of a naturally no-ELM or small-ELM regime include plasma shaping, plasma rotation (toroidal rotation and $\mathbf{E} \times \mathbf{B}$ rotational shear), the ∇B drift configuration and the local magnetic shear.

Fig. 1 shows the relative ELM energy loss normalized to the pedestal energy, $\Delta W_{ELM}/W_{ped}$, as a function of the pedestal electron collisionality [17], including the parameter space of the I-mode and the X-point radiator regime, recently established at JET [34] and AUG [48]. Compared to the standard type-I ELMing H-mode (in red) and considering the ELM size scaling [49], the small-ELM or no-ELM solution appears as potential candidate for future pulsed fusion devices, such as ITER or EU-DEMO.

Here, we review the latest developments of several no-ELM and small-ELM regimes and discuss their potential to integrate an edge solution while preserving high confinement in the core. To assess whether each scenario is applicable to future fusion devices, we will map out the experimental parameter space using a star chart (see Section 4), keeping in mind that there are other hidden parameters and all elements are important to achieve a core–edge integrated scenario. Note also that in present day machines some parameters of the star chart cannot be achieved simultaneously, e.g. low pedestal collisionality and high separatrix density cannot be achieved at once and can only be studied in separate experiments. ITER will play a key role to verify the core–edge integration of a no-ELM or small-ELM alternative.

3. High confinement regimes without large type-I ELMs

3.1. I-mode

Early observations of the improved energy confinement mode were obtained in the late 1990s on Alcator C-mod [24] and AUG [23], and were intensified in the late 2000s when the regime was named I-mode [25]. The I-mode is typically accessed in the unfavourable ∇B drift configuration, with the ion ∇B drift pointing away from the active X-point, and characterized by a higher power threshold to access H-mode compared to the favourable configuration. The I-mode features L-mode like particle transport levels while the energy confinement is enhanced, manifested in the build-up of a temperature pedestal [50]. The differences in the transport channels of the I-mode were recently reproduced with gyrofluid simulations [51,52] and explained by the dynamics parallel to the magnetic field. The model reproduces the main features of the I-mode via stabilization of the ion temperature gradient mode at the very edge of the plasma. Thus, drift-wave turbulence can become dominant and can lead to a decoupling of density and temperature fluctuations through the parallel heat conduction [51]. Recent BOUT++ simulations reproduce the main I-mode characteristics and highlight the importance of the E × B Doppler shift in inducing a change in the cross-phase between the electric potential and density fluctuations [53]. Further verification of both model assumptions against experiments are needed.

I-mode plasmas are inherently devoid of any type-I ELM as the I-mode pedestal is peeling-ballooning stable [54,55]. Instead of ELMs, the I-mode is characterized by a weakly coherent mode (WCM) which dominates the turbulence spectrum in I-mode, though recent measurements have also shown that it does not appear exclusively in I-mode at AUG, but can appear also during the L-mode [56]. Further, the I-mode has good impurity transport properties [57] and no impurity accumulation is observed when entering the I-mode. The L-I power threshold scales with density and a weak dependence on the toroidal magnetic field is found [58,59]. Owing to the stronger dependence of the L-H threshold with magnetic field, the I-mode existence window widens considerably when going to higher magnetic field strength [58] and should be further explored in high field tokamaks, such as the next-generation tokamak SPARC [60–62]. The higher power threshold to access the I-mode compared to the standard L-H power threshold in the favourable configuration, $P_{L-H,fav}$, is a challenge for ITER and EU-DEMO. In addition, operation at reversed field is not straightforward in ITER as it implies neutral beam operation in counter-current direction. In ITER, the PFC surface shaping assumes a certain magnetic field line helicity. To operate ITER with reversed toroidal magnetic field, B_t, implies that also the plasma current, I_p, must be reversed and thus, the beams are injected in counter-current direction.

At lower density (below the minimum of the L-H power threshold of the favourable configuration, e.g. for AUG below $3.5 \cdot 10^{19}$ m^{-3}), the L-I power threshold (i.e. with the ion ∇B drift pointing away from the active X-point) reaches similar values as $P_{L-H,fav}$ [59], thus opening a possible I-mode entrance in future fusion devices. Initial experiments on the I-mode access in the favourable configuration have been carried out on Alcator C-Mod [63] and AUG [64], but the results are not conclusive yet, and the operating space for the regime appears narrower.

The I-mode has been observed on Alcator C-Mod [25,58], AUG [23], DIII-D [65], EAST [66,67] and recently also on KSTAR [68], indicating that the I-mode is independent of the wall material. Whether a correlation of the quality of the edge thermal barrier in I-mode with metal walls is present should be studied and compared to I-modes in carbon wall machines. The I-mode has also been accessed with electron cyclotron resonance heating (ECRH), ion cyclotron resonance frequency (ICRF) heating, lower hybrid current drive (LHCD) and neutral beam injection (NBI) heating. Recently, NBI heated I-modes were extended to stationarity employing β_{pol} feedback control [56], with β_{pol} being the ratio between the plasma kinetic pressure and the magnetic pressure with respect to the poloidal magnetic field.

Analysis of the divertor radiation also enabled to differentiate between 'quiet' I-modes without any divertor radiation fluctuations, 'bursty' I-modes with intermittent bursts at the plasma edge [69] and I-modes with pedestal relaxation events (PREs) [70,71] that appear when approaching the transition from I-mode to H-mode and thus, can be used as indicator to show the proximity to the H-mode. They were observed on AUG with a W wall [70] and on Alcator C-Mod [71]. As the name indicates, they cause a relaxation of the edge electron profiles and have a characteristic frequency, ELM-like divertor signatures and timescales. The energy loss relative to the plasma stored energy induced by PREs is about 1% and is thus, lower compared to type-I ELMs at the same pedestal collisionality [70]. The transport increase caused by the PRE might be explained by a sudden jump in the cross-phase between electron temperature and plasma potential fluctuations [52]. In addition, PREs are different from type-I ELMs as ideal MHD stability analysis indicates that the I-mode PRE operation point is far away from the peeling-ballooning stability boundary [70]. The PREs were recently also observed in H and He plasmas at AUG [72]. Moreover, similar events named pedestal burst instabilities were also recently found at EAST [73].

The integration of a power exhaust solution was also studied in I-mode [74,75]. On Alcator C-Mod, impurity seeding using N to reach detachment in I-mode showed a deleterious effect on the confinement [74]. In fact, an I-L back-transition, shortly after nitrogen was introduced into the private flux region, was observed with no signs of divertor detachment. In I-mode, impurity seeding was observed to lower the pedestal top temperature ultimately leading to the transition back into L-mode. This result was confirmed by ECRH heated I-modes on AUG. However, when applying the same strategy in NBI-heated plasmas using β_{pol} feedback and applying N seeding already during the L-mode phase, detachment of the inner divertor leg was achieved for the first time in I-mode [75], see Fig. 2. In this case, the inner divertor detached while the plasma was still in L-mode and then transited into an I-mode (as the set β_{pol} value was slowly increased). The inner divertor leg remained detached during the L-I transition and during the I-mode, maintaining also the good confinement of the I-mode. During the whole experiment, the outer divertor leg remained attached [75]. To date, the integration of the I-mode with a complete power exhaust solution is still an outstanding challenge and further experiments are required.

3.2. QH-mode

The QH-mode was originally observed on DIII-D [26], and subsequently also obtained at AUG [76], JET [77] while still equipped with a carbon wall, and JT60-U [78,79]. The quiescent H-mode (QH-mode) is a high-performance, no-ELM scenario that features a fully developed density and temperature pedestal at low collisionality. Here, the type-I ELMs are replaced by an edge harmonic oscillation (EHO), a coherent MHD mode of kink-peeling nature [26,27]. The early work on the QH-mode is now also referred to as standard QH-mode, as recently a wide-pedestal variant of the QH-mode was discovered [80–82] (see below).

The edge rotation and E × B shearing rate was identified to be a key parameter for accessing the standard QH-mode [77,82,83]. This was confirmed in torque ramp experiments at DIII-D, demonstrating that the EHO appears above a critical E × B shearing rate threshold. When the E × B shearing rate is too low, the EHO disappears and the ELMs come back. The critical E × B shearing rate can be achieved with NBI in co- and counter-direction [84]. The studies were recently also extended to zero net torque by replacing the injected beam torque with non-resonant torque driven by 3D magnetic perturbations [82].

When performing the torque ramp experiments at higher triangularity, in balanced double null plasmas, a new variant characterized

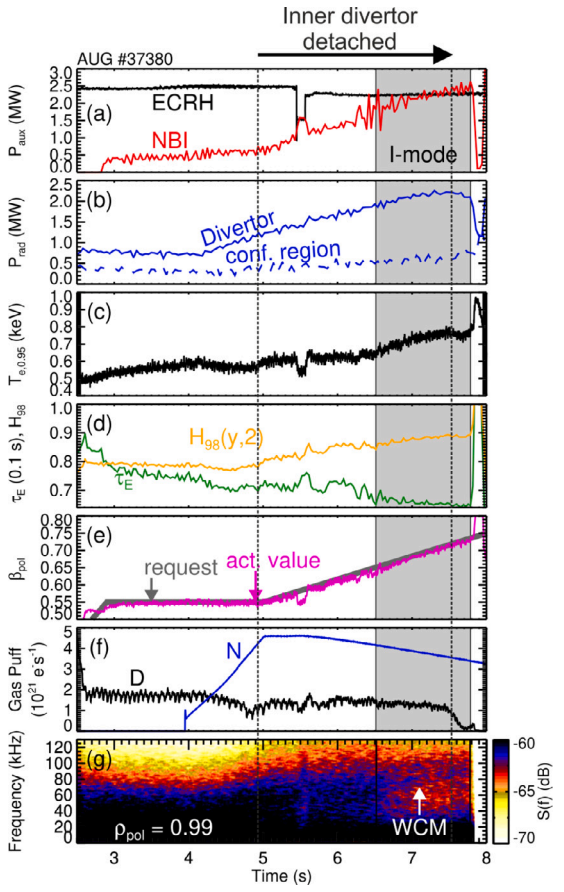

Fig. 2. Compatibility of the I-mode with a detached inner divertor. The inner divertor was detached during the L-mode phase by applying N seeding, the plasma entered I-mode at 6.52 s which was maintained until 7.82 s.
Source: Reproduced from [75].

by broadband MHD oscillations has been observed at DIII-D and was dubbed wide-pedestal QH-mode (WPQH) [80–82]. The WPQH features a larger pedestal width, a higher pedestal height (up to 60% increase) and higher energy confinement (up to 40% increase) compared to the standard QH-mode at comparable engineering parameters. In the wide-pedestal case, the steep gradient region is shifted inwards compared to the standard QH-mode, i.e. maximum gradients and E × B shearing are located further inside. Further outwards, closer to the separatrix, where the standard QH-mode locates its steep gradient region, the profiles are flatter and the E × B shear is reduced [80]. The modified E × B shear induces changes in the edge MHD activity, thus, in transport, ultimately leading to a wider pedestal. Along with rotation, a key ingredient to access this regime is shaping, and the WPQH was recently also observed in single null plasmas [85,86]. It also has better performance qualities at low torque and was recently accessed and sustained with zero net torque using non-axisymmetric magnetic perturbations to induce a neoclassical toroidal viscous (NTV) torque [87]. The WPQH was also sustained with dominant electron heating (up to 77% of on-axis ECRH) without any significant confinement degradation [88].

Compatibility with high pedestal top density was achieved by gas puffing into a standard QH-mode at DIII-D [89]. ITER target values were achieved (up to Greenwald fractions of 0.8), albeit transiently, requiring more studies to demonstrate the compatibility of the QH-mode with high Greenwald fractions and dissipative divertor states. At JET-C, the EHO was observed in stationary QH-mode plasmas with Greenwald fractions up to 0.6 [77].

At higher density, the EHO is often replaced by broadband MHD oscillations [89]. Too much puffing can lead to a loss of density control, and ultimately to loss of the QH-mode. Preliminary studies on the compatibility of the QH-mode with a radiative divertor were carried out at DIII-D showing that the QH-mode can be maintained with small levels of impurity injection [90,91]. These studies are at a nascent stage and require dedicated experiments to study whether the QH-mode is compatible with a power exhaust solution.

In standard QH-modes, the impurity transport due to the EHO was observed to be faster than that caused by ELMs at similar conditions [92–94]. In plasmas which feature a type-I ELMing phase and then enter the QH-mode without ELMs there is a decrease in plasma density as the EHO sets on indicating increased main ion transport [26,76,95]. First impurity transport studies in the WPQH regime were carried out using laser-blow-off injection of aluminium [85]. In these experiments, no tendency for impurity accumulation was observed and the WPQH featured outward impurity convection. Impurity confinement times similar to standard ELMing H-modes have been observed. However, it must be noted that WPQH discharges have also been observed with significantly longer impurity confinement times. The differences are currently being investigated [85]. A database analysis of no-ELM scenarios at DIII-D also showed that, while the QH-mode features very high pedestal pressures and confinement, in some cases high effective charge, Z_{eff}, values are observed [96]. The increased edge impurity content is observed in cases with low net injected NBI torque and thus, may be related to carbon sputtering caused by using a counter-current beam. Understanding the impurity transport in QH-mode is of paramount importance to avoid these high Z_{eff} values and thus, fuel dilution.

The establishment of a QH-mode with a metal wall has proven to be more difficult than for the cases with a carbon wall described above. Plasma operation in a W wall environment such as AUG requires gas puffing and core ECRH to avoid W accumulation, both actions are not necessarily benevolent to establish and access the QH-mode. In the past years, dedicated experiments were carried out in ASDEX Upgrade to find a route to establish the QH-mode in AUG-W [97,98]. For the first time in a metal device, the EHO was observed in transient QH-modes with a duration up to 500 ms. The QH-mode was observed both with co-injected and counter-injected NBI, in both cases in the unfavourable configuration (upper single null with forward I_p/B_t and co-NBI, lower single null in reversed I_p/B_t and counter-NBI) featuring a higher L-H power threshold. In both configurations, ECRH was used to prevent core W accumulation, leading to a higher core electron temperature compared to the ion temperature [97]. This is one of the key differences from the QH-modes observed at AUG with the C wall [76,94]. While the EHO is mostly established with dominant NBI heating, it has recently also been observed in dominant ECRH heated plasmas at AUG [98]. Interestingly, an $n = 1$ edge mode with peeling nature also appeared in low pedestal collisionality experiments on Alcator C-Mod [99] and may be related to an EHO.

Fig. 3 shows an example from the AUG tokamak, in this case from the reversed I_p/B_t campaign. As the plasma transits into a higher confinement regime, two small ELMs appear, and then continues to evolve until, at 1.59 s, it arrives into a regime with a higher recycling level, as shown in one of the bolometry channels. At the same time, an EHO appears and the stored energy, plasma density and radiated power stall. The phase with the EHO lasts for 320 ms. At 1.827 s the plasma density starts to increase (by 10%), co-inciding with a shape change that also induces a change in q_{95} and evolves into a type-I ELMy regime at 1.92 s. As shown in Fig. 3, the EHO appears with 1.8 MW counter-NBI and up to 2.5 MW of ECRH.

Transient EHOs were recently also observed on JET [100] in dominant NBI heated discharges, however, more experimental studies in metal devices are required to extend the QH-mode to stationarity.

EAST recently also reported the observation of the QH-mode, in upper single null discharges with NBI, ECRH and lower hybrid heating [101]. In this case an edge mode appeared with low toroidal mode numbers (n = 1), however, at a higher fundamental frequency ($f \sim$

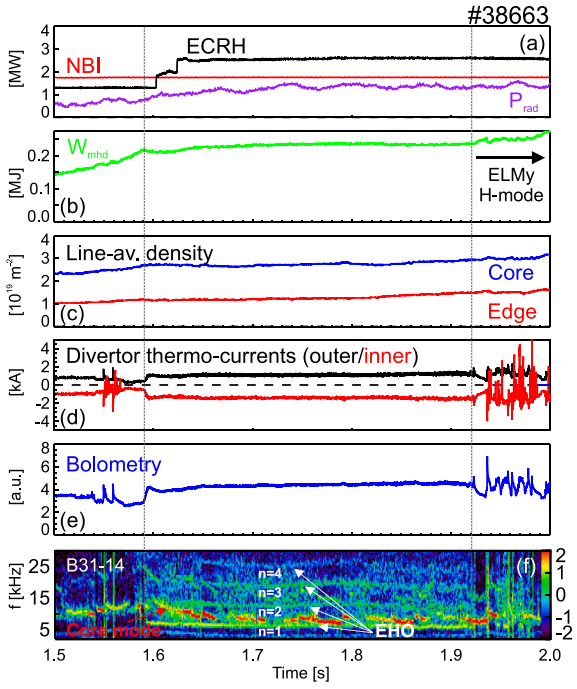

Fig. 3. Timetraces of QH-mode example at all-W AUG: (a) NBI (red), ECRH (black) and radiated power (purple), (b) stored energy (green), (c) line-averaged density in the plasma core (red) and edge (blue), (d) thermo-currents in the inner (red) and outer (black) divertor, (e) AXUV radiation measured by a bolometry channel indicated increased transport as the EHO sets on, (f) magnetic frequency spectrogram highlighting the onset of the EHO at 1.59 s. (For interpretation of the references to colour in this figure legend, the reader is referred to the web version of this article.)

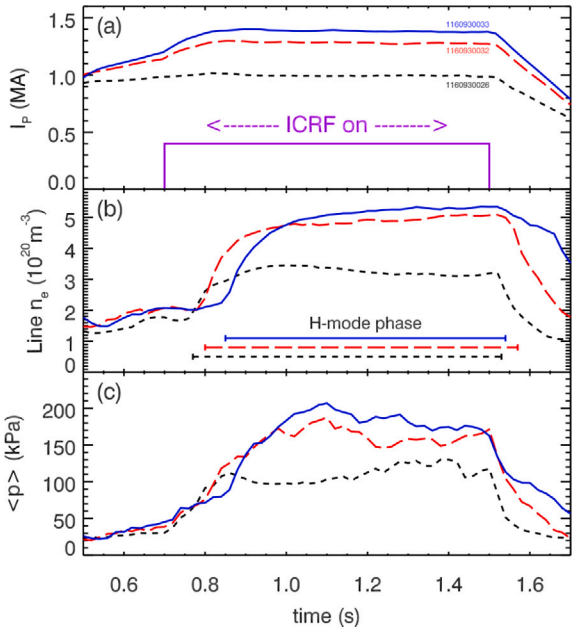

Fig. 4. Temporal evolution of (a) plasma current, (b) line-averaged density and (c) volume averaged plasma pressure for three EDA H-mode discharges. In (a) the time trace of the ICRF heating is shown in purple. (For interpretation of the references to colour in this figure legend, the reader is referred to the web version of this article.) *Source:* Reproduced from [99].

60 kHz) compared to EHOs observed at DIII-D, AUG or JET. Using non-axisymmetric perturbations an H-mode without the occurrence of type-I ELMs characterized by quasi-coherent and broadband MHD fluctuations was obtained with only RF heating [101].

3.3. EDA H-mode

The enhanced D-alpha high confinement mode (EDA H-mode) was originally discovered on Alcator C-Mod [28,29] with ICRF heating. It was reproduced on DIII-D [96,102] and EAST [103] and recently, also observed on AUG by applying fine scaled ECRH power scans [104]. The EDA H-mode is typically obtained in plasmas with favourable ∇B drift direction, high fuelling and high collisionality, with high density in the plasma core and pedestal and modest pedestal temperatures. It features stationary density without ELMs, high confinement and moderate impurity confinement times [57]. The onset of the EDA H-mode is characterized by the appearance of a quasi-coherent mode (QCM), localized at the plasma edge, that likely takes over particle and energy transport as it replaces the ELM. It is more likely found at high safety factor (q_{95} larger than 3.5), modest pedestal temperatures, higher density and higher triangularity [105], demonstrating again that plasma shaping can play a key role. At AUG, filaments with frequencies around 1 kHz are found to dominate the transport in the near scrape-off layer [106]. On Alcator C-Mod, when the edge temperature and pressure gradient increase, the QCM is replaced by broadband low frequency fluctuations and small, grassy ELMs are observed [107].

Operation at high triangularity allows a broader power window for accessing this regime at AUG, and also allows a direct entrance from L-mode into the EDA H-mode without going through a type-I ELMing H-mode [104], as observed at lower triangularity when small ECRH power steps are employed. At low triangularity, the power window for the existence of the sustained EDA H-mode in AUG is relatively small (~0.2 MW), thus requiring a very fine control of the input power. Operation with increased gas fuelling also helps to extend the power window of the EDA H-mode, at the same time a higher plasma density is achieved and the QCM is observed to broaden in the frequency spectrogram [108].

At AUG, the EDA H-mode has been observed in plasmas with edge safety factors of q_{95} = 4.8–6.9 on a routine basis [104]. Operation at low q_{95} is challenging, but has been obtained down to ITER target values of q_{95} = 3 at Alcator C-Mod albeit with relatively high pedestal collisionality. Recently, the EDA H-mode was also observed in the ITER baseline scenario, which adopts strong shaping $\delta > 0.3$, with $q_{95} = 3$ using ICRH and NBI heating at AUG [109]. The EDA H-modes are performed at a Greenwald fraction of ≈0.9–1.0. Note that in present day machines low pedestal top collisionality and high Greenwald fraction cannot be obtained in the same discharge.

During the last experimental campaign at Alcator C-Mod in 2016, the parameter space of the EDA H-mode was extended to 7.8 T [110] with the aim to maximize density by combining a large power input with low-Z impurity seeding, high plasma current and optimized fuelling. In EDA H-mode at 5.7 T, a world record average plasma pressure of more than 200 kPa was obtained at Alcator C-Mod, without the occurrence of any ELM [99] (see also Fig. 4).

The compatibility with a power exhaust solution has been demonstrated on Alcator C-Mod using impurity seeding (N, Ne, Ar) to reduce the divertor heat flux while maintaining high confinement [111,112]. In fact, the energy confinement factor, $H_{98}(y,2)$ remained larger than 1 as long as the net power was larger than the H-mode power threshold [111]. Ar seeding allows to obtain complete ELM suppression at low power going through the separatrix, as observed on AUG [113]. Using P_{sep} as control tool and Ar seeding as feedback actuator, the power window of the EDA H-mode at AUG was extended to higher levels and to combined NBI and ECRH heating, demonstrating also its compatibility with core-integration by means of Ar and N seeding [114]. Recent quasi-linear GENE simulations of an Ar seeded EDA H-mode [115] show that ITG-driven anomalous transport is reduced in the outer core when argon impurities are included.

3.4. Small ELM regimes

A variety of examples exist within the area of small-ELM regimes and date back to the early 1990s [30,31,116]. Small-ELM regimes typically show reduced ELM energy losses, smaller ELM amplitudes and higher ELM frequency. Many of the small ELM regimes, such as type-II ELMs at AUG and JET [30,31,117,118], type-V ELMs at NSTX-U [119] or grassy ELMs at DIII-D [116], JT-60U [120] and EAST [121,122], are obtained in highly shaped plasmas underlining the importance of triangularity for the stability of the pedestal. A grassy ELM regime has also been observed on EAST applying Ne seeding [123] (see also Section 3.5).

Recently, at JET, a new high-confinement, small-ELM regime was found in the baseline scenario (Baseline Small ELMs, BSE) at low q_{95} = 3, low pedestal collisionality, high current and magnetic field and optimized fuelling [124,125]. The regime is characterized by stationary density and radiation levels, high performance with high ion temperatures and no high-Z impurity accumulation was observed. It also features a wider density pedestal width, thus leading to a wider pressure width and improved pedestal stability. A reduction of turbulent transport at the plasma edge was observed, together with an increase in rotation and outward impurity convection were identified as key mechanisms to obtain this regime [124]. While Greenwald fractions up to 0.7 were observed in stationary BSE plasmas when partially replacing gas injection with pellet fuelling [124], the compatibility of this regime with a power exhaust solution, dominant electron heating and reduced torque are not yet clear.

Within the EUROfusion consortium, the type-II ELMy regime [30,117] has recently regained attention due to its compatibility with the separatrix conditions in ITER and with a boundary solution. The conditions are also close to the EU-DEMO target values [11]. The recipe to obtain small type-II ELMs is high fuelling to induce high density at the separatrix and increased plasma shaping (triangularity and elongation) almost up to a double-null plasma.

Experiments at AUG varying the fuelling between pellets and gas puff, while keeping the same pedestal top density, allowed to disentangle the effects between pedestal top and separatrix. At high separatrix density small type-II ELMs occurred while at low separatrix density type-I ELMs appeared, indicating that the conditions close to the separatrix are important to achieve these small ELMs [32]. As the small ELMs develop at high separatrix density, the density in the scrape-off layer is observed to increase and a density shoulder is formed. This may be attributed to modes that are activated close to the separatrix, causing enough transport that they lead to a local flattening of the gradient region, thus causing a flatter density profile around the separatrix. This effectively leads to a narrower pedestal, which is more stable against peeling ballooning modes and type-I ELMs are replaced with small type-II ELMs that lead to quasi-continuous exhaust [126]. Thus, this regime is also referred to as the quasi-continuous exhaust (QCE) regime. At TCV, the QCE regime was recently also established using a highly triangular plasma ($\delta \sim 0.6$), reaching almost a double null configuration [33]. A comparison of a low and high triangularity discharge at TCV is shown in Fig. 5 [33]. While the low triangularity plasma (in black) develops type-I ELMs, the high triangularity case (red) shows small ELMs, or, QCE bursts.

Comparison of the heat flux profiles on the target, measured with infrared thermography in the QCE regime and standard type-I ELMing H-modes at ASDEX Upgrade, shows that the QCE regime features a broader power fall-off length, λ_q, up to a factor of 4, resulting ultimately in reduced peak heat fluxes on the divertor [127]. The broadening of the λ_q does not degrade the confinement. A correlation between the λ_q broadening and higher filament frequency and radial propagation velocity is observed [106]. The increased filamentary activity may be related to the onset of ballooning modes close to the separatrix.

Ideal ballooning stability analysis of the QCE regime, in comparison to a type-I ELMy H-mode, showed that with increased gas puff and higher separatrix density, the plasma becomes more ballooning unstable at the bottom of the pedestal [128]. Increasing the gas puff has an effect on the pressure gradient but can also modify the equilibrium. Both the changes in the pressure gradient and the local magnetic shear lead the plasma to be close to the ideal ballooning stability limit at the pedestal foot [128].

Non-linear magnetohydrodynamic simulations with JOREK corroborate this hypothesis [5]. The QCE regime was reproduced in the simulations when the separatrix density was high enough. The type-I ELMs were replaced by small peeling-ballooning modes, with dominant

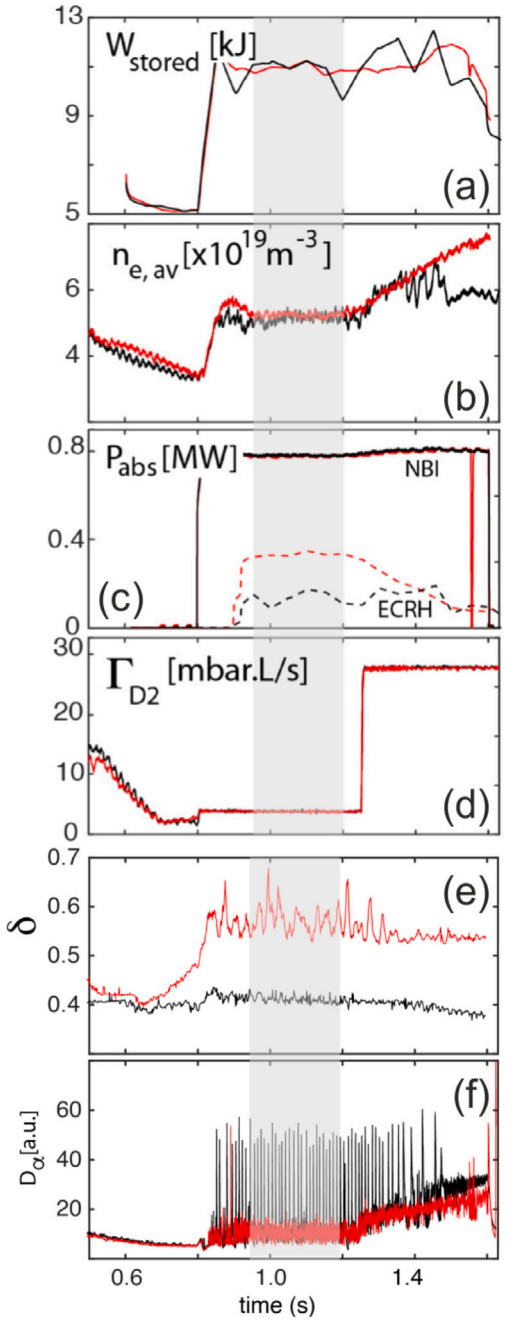

Fig. 5. Timetraces of QCE discharge at TCV: (a) stored energy, (b) line-averaged density, (c) auxiliary heating power, (d) gas puff, (e) average triangularity, (f) ELM monitor showing that the high triangularity case (red) features small ELMs, while the low triangularity case (black) has large type-I ELMs. (For interpretation of the references to colour in this figure legend, the reader is referred to the web version of this article.)
Source: Reproduced from [33].

ballooning mode nature, that cause constant levels of outwards transport, thus preventing the build-up of the pedestal up to the type-I ELM stability limit. These modes were observed in the outermost 5% of the confined plasma region [5].

Using a double feedback control on β_{pol} via a NBI power ramp and on the divertor temperature using nitrogen seeding, the QCE regime was entered directly at high safety factor ($q_{95} = 5.5$), without the occurrence of any large type-I ELM [127,129]. In these plasmas, a partially detached divertor was achieved (i.e a divertor electron temperature $T_{div} < 10$ eV across the outer divertor target is achieved [13]), while the filaments were observed to remain attached (i.e. during the filamentary transport $T_{div} > 10$ eV).

3.5. ELM suppression via impurity seeding

Extrinsic impurity seeding enables the reduction of heat fluxes onto the divertor target plates as a major part of the power flux is converted into radiation, thus facilitating divertor detachment [13,14]. At the same time, impurity seeding can also affect the ELM response and the pedestal structure [47,130]. In nitrogen seeded plasmas, the ELM frequency is increased while the ELM duration and amplitude are decreased. These plasmas also feature a reduced separatrix density, which can lead to an inward shift of the maximum pressure gradient and, therefore, enhanced pedestal stability [130].

At JET, a stationary no-ELM regime with high performance, reduced heat loads to the divertor and high radiated fraction was found with neon seeding in ITER relevant conditions (low pedestal collisionality, 2.7 T, 2.5 MA, $q_{95} = 3.2$, $\delta = 0.38$) [34]. High confinement up to $H_{98}(y,2) = 1.0$ and high pedestal temperatures ($T_e = 1$ keV, $T_i = 1.2$ keV) are obtained in stationary conditions without impurity accumulation, at moderate neon concentrations (1.3%), moderate $Z_{eff} = 2.7$ and Greenwald fraction of 0.5 [34,131]. In contrast to previous results at lower heating power, in which Ne seeding had worse performance compared to N seeding [132], the new experiments with 28 MW of NBI power show that Ne seeded plasmas achieve higher energy confinement factors and higher neutron rates at the same plasma energy [131,133] (see also Fig. 6). This is partly ascribed to higher pedestal density and lower pedestal temperatures in N seeded plasmas [132].

When the pronounced detachment state is achieved by applying strong impurity seeding, the radiation is localized in a small region close to the X-point inside the confined plasma [48,134,135]. The X-point radiator (XPR), a dense, cold and strongly radiating volume close to the X-point inside the confined region, has been observed at JET with N, Ne and Kr seeding [48,132]. At AUG it has been achieved with N and Ar seeding [35,48] with a radiated power fraction close to 100%, and exists over a wide range of heating power (2.5 - 26 MW, corresponding to a ratio of 1–5 when normalized to the L-H power threshold). A model for the XPR based on the power balance of the XPR volume was recently developed and highlights the importance of high neutral and edge plasma densities as well as low power crossing the separatrix, P_{sep} [136].

At AUG, a direct correlation between the location of the X-point radiator and the level of detachment is observed [35], which can be influenced by the level of heating power or impurity seeding. Thus, the signature of detachment of the outer divertor can be used to identify the start of the XPR. A real-time control tool was recently implemented at AUG [35] using the AXUV diode measurements of the XPR as sensor, while the impurity seeding level (N or Ar) or the heating power levels acts as actuator. A radiation position of up to 10 cm above the X-point was actively controlled [35]. For XPR locations higher than 7 cm, the ELMs disappear and the plasma enters a stationary ELM suppressed regime (XPR no-ELM regime). In this regime, the stored energy decreases by about 10% ($H_{98}(y,2) \approx 0.95$), while the density is reduced by 15%, and the outer divertor remains fully detached. Compared to the ELMing XPR phase, the pedestal gradients are shallower [35]. Nitrogen

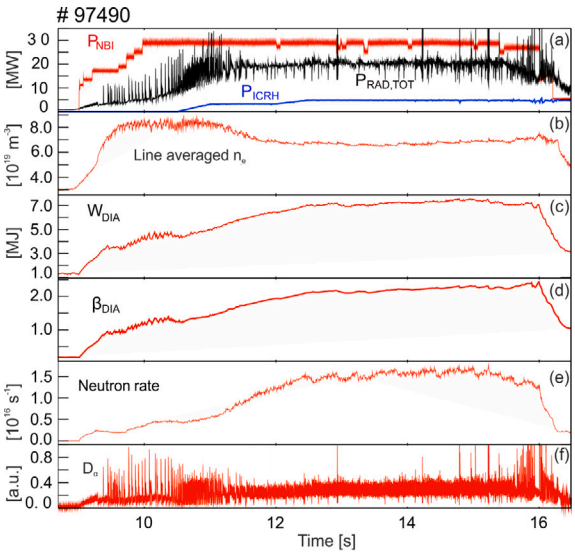

Fig. 6. No-ELM regime using Ne seeding at JET: (a) auxiliarity heating (NBI power and ICRF power) and radiated power, (b) line-averaged density, (c) stored energy, (d) plasma β, (e) neutron rate, (f) ELM monitor.
Source: Reproduced from [34,133].

concentrations between 2–3.5% were observed, with Z_{eff} values up to 2.5. Despite the absence of ELMs, no core impurity accumulation is observed, thus making this a very promising regime for future fusion devices as it is inherently compatible with a power exhaust solution. Compatibility with high pedestal top temperature and low pedestal collisionality requires higher pedestal pressure to be demonstrated.

A similar control tool was recently also developed on EAST to maintain a grassy ELMy H-mode using Ne seeding [123]. In this case a multi-feedback control scheme is employed, which uses Langmuir probe measurements of the electron temperature to identify the onset of detachment and then switches to feedback control on measurements of an AXUV diode viewing the X-point region to track the radiation level at the X-point. Here, the feedback control is performed on a piezo valve that controls the amount of neon injection [123]. This combined control scheme may be employed to independently control power exhaust during the ramp-up, flat-top phase and ramp-down of the plasma discharge.

3.6. Negative triangularity L-modes

In recent years, the negative triangularity (NT) shape has regained attention as a potential alternative to conventional no-ELM regimes as it features high performance with an L-mode edge and thus, is inherently devoid of type-I ELMs [137,138]. It also facilitates power exhaust as NT naturally places the X-point at the low field side and thus, a larger wetted area over which the power can be distributed is achieved. This makes NT L-modes very attractive and they are considered as an option for future fusion reactors [139,140].

Discovered originally at TCV in the 1990s [36], NT ohmic plasmas featured a better confinement compared to their positive triangularity (PT) counterparts. An increase in confinement was observed when going to very small positive triangularity [37]. When applying ECRH, the NT L-modes showed the same plasma profiles as in PT, but at half the heating power [141]. In this case, the electron energy confinement time increased by a factor of 2. The experiments showed a decrease in the experimental electron heat diffusivity, χ_e, with increasingly negative triangularity (stronger shaping) and increasing plasma collisionality [141]. Fluctuation measurements based on the correlation electron cyclotron emission diagnostic confirm this result,

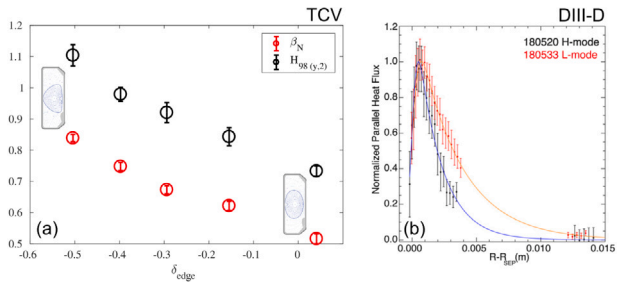

Fig. 7. (a) Confinement factor $H_{98}(y,2)$ and normalized plasma β_N as a function of increasing NT values (reproduced from [144]). (b) Comparison of parallel heat flux profile measured with infrared thermography in NT plasmas at DIII-D: L-mode case (red), H-mode case (black). The NT L-mode features a wider power fall-off length compared to a NT H-mode. (For interpretation of the references to colour in this figure legend, the reader is referred to the web version of this article.)
Source: Reproduced from [140].

the fluctuation amplitude at the plasma edge strongly reduces in NT plasmas [142].

Comparing PT and NT with the same heating power level, higher core electron and ion temperatures, at similar densities, are observed in NT [143], and thus, a higher plasma stored energy is achieved. This was observed in both ECRH and NBI heated plasmas. To date, no clear confinement saturation was found at TCV [144], the core confinement factor $H_{98}(y,2)$ and normalized plasma β_N increase with increasingly more negative triangularity (stronger shaping) (see Fig. 7(a)).

Recent experiments at DIII-D extended NT investigations to dominant NBI heated plasmas in limited and diverted configurations [140,145]. Comparison of the NT and PT shapes at otherwise similar plasma parameters (plasma current, toroidal magnetic field, plasma density and auxiliary heating), shows that the NT L-mode achieves similar performance as the PT H-mode despite lacking a pedestal. Normalized plasma β_N up to 3 and energy confinement factors up to 1.2 were achieved in NT L-modes [96,140,145]. The NT reference also featured lower impurity content and no core impurity accumulation despite the absence of ELMs. Impurity transport studies at DIII-D using Al and F laser blow-off injection show short impurity confinement times, high diffusion and low convection transport coefficients in the plasma core, resulting in low impurity retention [146]. On the contrary, at TCV, NT plasmas featured a higher carbon density compared to their positive counterpart and showed accumulation of C ions around mid-radius [147].

AUG recently also developed a NT shape and achieved average triangularities down to −0.19 [148,149]. Pure ECRH heated NT plasmas show high energy confinement similar to PT H-mode plasmas with $H_{98}(y,2)$ up to 1, however, in plasmas with mixed heating (NBI, ECRH and ICRF), when taking into account fast-ion corrections, reduced confinement is observed ($H_{98}(y,2) \approx 0.6$) [149]. Both plasma scenarios feature a power degradation similar to H-modes at PT [148]. Operation in unfavourable configuration was found necessary to avoid the transition into H-mode in NT. In the favourable configuration, the H-mode was obtained in NT with a reduced pedestal and more benign ELMs with higher frequency and smaller amplitude [149], similar to observations at DIII-D [140].

Analysis of the pedestal stability [150,151] confirms the experimental observation and shows a reduced pedestal height when scanning the triangularity from PT to NT. The degradation of the peeling-ballooning stability was attributed to the fact that the second stability region for ballooning modes closes for NT shapes, limiting the edge pressure gradient to the ballooning stability limit [150–152]. Access to the second stability region is only possible above a certain critical triangularity threshold and when the local shear in the bad curvature region is sufficiently negative [152].

The absence of ELMs in a high confinement NT L-mode makes this regime very promising for future fusion devices. In addition, a broader heat flux profile is found in NT L-mode compared to NT H-mode (as in PT plasmas) which is beneficial in terms of power exhaust [140]. Fig. 7(b) shows a comparison of the parallel heat flux profile in NT L-mode and H-mode measured at DIII-D [140]. An L-mode database at TCV shows that the power fall-off length, λ_q, measured on the outer divertor target scales with the triangularity, however, with smaller λ_q at NT [153]. Extension to an H-mode database and comparison of the heat flux profile and power fall-off lengths in NT L-modes and PT H-mode counterparts should be envisioned to ensure integration with a boundary solution.

The implementation of radiative cooling to mitigate power exhaust onto the divertor is also easier in an L-mode as no requirement on the power crossing the separatrix is needed. However, compatibility of NT plasmas with divertor detachment and high radiated power fraction has yet to be demonstrated. While NT L-modes has many beneficial properties for future fusion devices, its attractiveness is somewhat less well established and further studies are needed to show that the confinement improves in ITG dominated NT plasmas (ideally both in carbon and metal machines).

4. Discussion and experimental parameter space

To map out the experimental parameter range of the individual confinement regimes discussed in Section 3, we employ a star chart highlighting key elements that are needed in future fusion devices. The figure of merit is similar to [21], extended with the radiation fraction. The star charts presented in Fig. 8 shows the pedestal Greenwald fraction $f_{GW,ped}$, the inverse ion collisionality in the pedestal, average triangularity, inverse edge safety factor q_{95}, β_{pol} and radiation fraction f_{rad}. For reference we also plot the target values for ITER [154] and the EU-DEMO baseline scenario [11]. Note that in present day machines, several parameters in the star chart cannot be achieved simultaneously, e.g. a high Greenwald fraction and low collisionality cannot be obtained at the same time. To further highlight this, we have also included the values for the individual experiments of each regime, discussed in the previous sections, with a white dashed line. It should also be noted that not all challenges and unknowns are captured in this star chart. The nature of the underlying mode, the role of Z_{eff} and impurity transport in general [155], divertor detachment [14], compatibility with pellet injection [41,42], the role of energetic particles [6], extrapolations to high Q operations play an important role for future fusion devices.

While the I-mode is an attractive no-ELM solution with high performance and compatible with many key elements necessary for future fusion devices (such as dominant electron heating, low torque, metal wall), it also features outstanding challenges. The compatibility of the I-mode with a full power exhaust solution remains elusive, despite recent promising results on the detachment of the inner divertor leg at AUG [75]. In addition, operation at higher edge densities and higher Greenwald fractions as well as higher power levels still needs to be demonstrated. The high L-I power threshold due to the unfavourable drift configuration is a concern for future fusion devices, as it requires higher P_{sep} compared to a type-I ELMing H-mode scenario. This may be solved at sufficiently high magnetic field, one of the objectives of SPARC. An alternative option may be to enter the I-mode at lower density and/or lower magnetic field and then ramp up the density. However, the divertor challenge still remains and requires further studies.

The QH-mode features very high performance and covers a wide existence range in terms of collisionality, triangularity, q_{95} and β_{pol}, as shown in Fig. 8(b). Here, the standard QH-mode is shown in red, while the WPQH regime is highlighted in purple. Note that the range covered by WPQH plasmas represents the values achieved in experiment to date and the physics limits have yet to be identified. The impurity transport needs to be assessed in more detail, in particular whether high

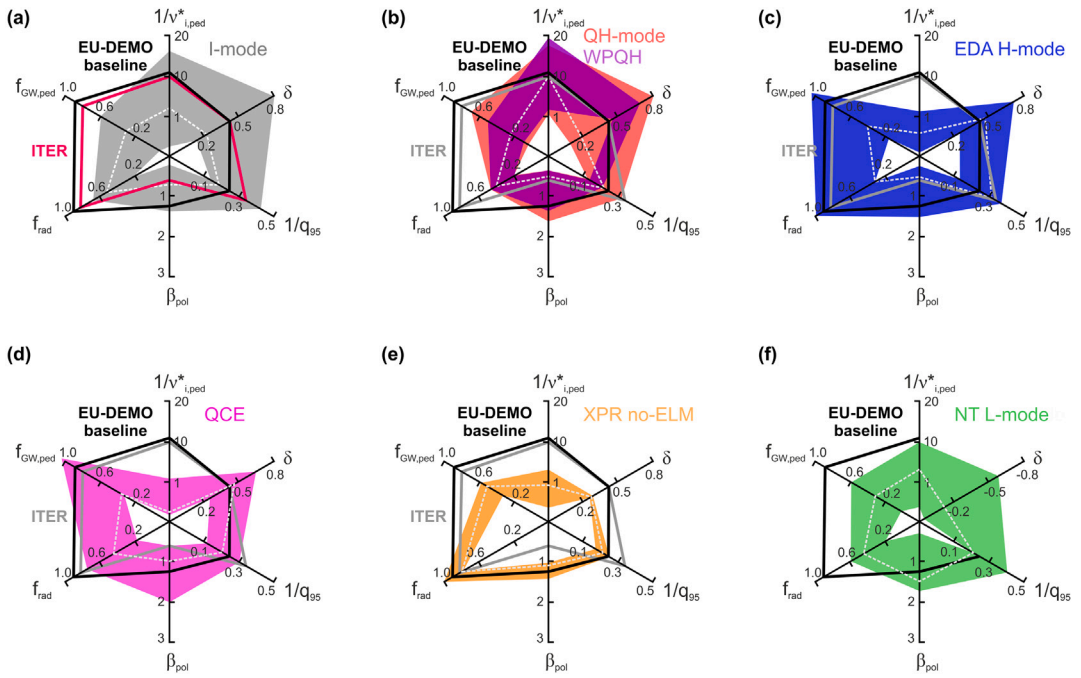

Fig. 8. Figure of merit displaying six axes (in clockwise direction), the inverse ion collisionality in the pedestal, average triangularity, inverse edge safety factor q_{95}, β_{pol}, radiation fracton f_{rad} and pedestal Greenwald fraction $f_{GW,ped}$: (a) I-mode, (b) QH-mode (standard QH-mode in red, WPQH in purple), (c) EDA H-mode, (d) QCE regime, (e) XPR no-ELM regime, (f) NT L-mode. For reference the ITER and EU-DEMO target values are shown. Notice that in (f) the average triangularity axis has negative values. Note that the white dashed line corresponds to each individual discharge discussed in the previous sections of the various regimes. This demonstrates an example of the level to which the parameters have been achieved "simultaneously" in a single plasma in present day devices. As the XPR no-ELM regime represents only AUG data, a representative AUG XPR discharge (#40 759) is shown. (For interpretation of the references to colour in this figure legend, the reader is referred to the web version of this article.)

performance discharges can be obtained with a reduced Z_{eff} value. While the study of QH-mode has recently been revived at AUG and JET with a metal wall, the compatibility of a sustained QH-mode in a W environment still needs to be demonstrated, and further experiments should be carried out in metal devices. The QH-mode access condition of a critical E × B shearing rate should be studied in detail, in particular, it should be clarified whether the outer or inner E_r shear region (or possibly both) play a role. Can this criticality condition also be achieved in plasmas with dominant wave heating? Is the level of torque required acceptable for future fusion devices? In this regard, the wide-pedestal QH-mode offers a low-torque high-performance alternative [87] and has also been sustained with dominant wave heating [88]. Further, outstanding challenges include steady QH-mode operation at higher divertor density as well as demonstrating the compatibility with a power exhaust solution. As the tolerance level of the QH-mode to intrinsic low-Z impurities is rather high, it may also be beneficial for core–edge integration via impurity seeding.

The EDA H-mode features many of the desirable properties of a future fusion device (operation at high Greenwald fraction and high radiated power fraction, compatibility with dominant electron heating, metal wall and accessible at low input power and torque), but outstanding challenges include the demonstration of its access at lower collisionality and higher power levels. Fig. 8(c) shows the parameter space for the EDA H-mode. While a rise in triangularity as well as feedback control on P_{sep} via Ar seeding enlarges the power window at AUG to access and sustain the EDA H-mode, a full control avoiding the transition into an ELMing H-mode is to be demonstrated. On Alcator C-Mod, at high β, small, grassy ELMs are observed [99,107].

Exchanging type-I ELMs with smaller and more benevolent ELMs may open the path to employ an H-mode scenario in future fusion devices. In this regard, the QCE regime is a promising scenario as it features high confinement with small-amplitude and high frequency ELMs (QCE bursts) and is compatible with high separatrix density operation. Fig. 8(d) shows the existence range so far obtained at AUG and TCV. As shown, outstanding challenges include the compatibility with low collisionality, access to this regime at low q_{95} and extension towards higher radiation fractions. To date, it is not yet clear how small an ELM has to be acceptable for EU-DEMO, taking into account the duration of the discharge and associated erosion of the divertor target plates [10] and requires further investigation.

Projecting towards future fusion devices, impurity seeding is an attractive control tool for ELM suppression. The XPR no-ELM regime combines high confinement with a power exhaust solution. It enables full detachment control at high dissipated power fractions (up to 95%). Fig. 8(e) shows the current operational space of the XPR no-ELM regime for AUG [35]. In view of ITER and future fusion devices, outstanding challenges include the compatibility of this regime with low pedestal collisionality and $q_{95} = 3$. Recent results from JET demonstrate that a neon-seeded, ELM suppressed regime can be obtained in ITER relevant conditions. Extension of the XPR no-ELM regime towards higher densities also remains to be demonstrated.

NT L-modes feature many advantages for future fusion reactors. They operate in L-mode, and as such, inherently avoid operation close to the ELM boundary. In addition, power exhaust should be easier to be implemented, as NT plasmas feature the X-point at the low field side and a larger wetted area for the power distribution can be achieved. However, this has not been demonstrated yet. Outstanding challenges, besides the integration with a boundary solution to mitigate power exhaust, include the vertical stability of the plasma. NT plasmas feature reduced MHD stability [156] and access ideal current driven modes at lower normalized plasma current. In addition, the predicted stability to the $n = 0$ Resistive Wall Mode limits the maximum elongation to be achieved at NT. The plasma beta limit also needs to be studied in more detail. To date, NT plasmas have achieved up to $\beta_N \approx 3$ with high confinement and are, in terms of core performance, comparable to other high confinement no-ELM regimes [96]. The confinement improvement in ITG dominated plasmas is, however, to date, not clear [149] and needs further studies to address this question.

While experimental studies can tackle many points discussed above, it is of paramount importance to provide a detailed physics understanding of each regime. Analytical models, extended MHD models,

gyrofluid and/or gyrokinetic simulations capture many of the physics aspects, but we are still lacking many details to be able to close the knowledge gaps for future fusion devices. One of the key questions to separate is whether a low pedestal collisionality or a high separatrix density/collisionality is the key driver of the regime (or whether both are important). In addition, the role of the underlying dominant mode or fluctuation in each regime for energy and particle transport needs to be assessed. This may also help to design strategies for core–edge integration and study the compatibility of a dissipative divertor.

5. Summary

Within the area of developing high performance scenarios without large type-I ELMs, substantial progress has been made in the past years. While historically some regimes have focused on core performance, and others on the boundary solution to mitigate the power exhaust problem and guarantee safe and steady-state divertor operation, it has become clear that for future fusion devices both need to be implemented and full core–edge integration is mandatory. Currently, none of the presented regimes can be selected or turned down as main candidate for a future DEMO like device as further work on closing the knowledge gaps is necessary.

In the fusion landscape, ITER, SPARC, JT60-SA and other machines that will come online in the next years will play a key role in unravelling the solution for a future tokamak reactor.

Declaration of competing interest

The authors declare the following financial interests/personal relationships which may be considered as potential competing interests: Eleonora Viezzer reports financial support was provided by European Consortium for the Development of Fusion Energy. E. Viezzer reports financial support was provided by European Research Council. E. Viezzer reports financial support was provided by BBVA Foundation. J. W. Hughes and A. E. Hubbard report financial support was provided by US Department of Energy.

Data availability

Data will be made available on request.

Acknowledgements

The first author would like to thank the referees and Dr. A. Pochelon for their valuable input. This work has partially been carried out within the framework of the EUROfusion consortium, funded by the European Union via the Euratom Research and Training Programme (Grant Agreement No. 101052200 – EUROfusion). Views and opinions expressed are however those of the author(s) only and do not necessarily reflect those of the European Union or the European Commission. Neither the European Union nor the European Commission can be held responsible for them.

E. V. and D.J.C.Z. gratefully acknowledge funding from the European Research Council (ERC) under the European Union's Horizon 2020 research and innovation programme (grant agreement No. 805162). The support from the 2020 Leonardo Grants for Researchers and Cultural Creators of the BBVA Foundation is gratefully acknowledged. The BBVA Foundation is not liable for the opinions, comments and contents included in the project and/or the results derived from it, being sole and exclusive responsibility of its authors. E. V. gratefully acknowledges funding from the Princess of Girona Foundation.

A. E. H. and J. W. H. gratefully acknowledge funding from the US DoE Award DE-SC0014264.

References

[1] F. Wagner, et al., Regime of mproved confinement and high beta in neutral-beam-heated divertor discharges of the ASDEX tokamak, Phys. Rev. Lett. 49 (1982) 1408.
[2] H. Zohm, Edge localized modes (ELMs), Plasma Phys. Control. Fusion 38 (1996) 105.
[3] A.W. Leonard, Edge-localized-modes in tokamaks, Phys. Plasmas 21 (2014) 090501.
[4] G.T.A. Huysmans, O. Czarny, MHD stability in X-point geometry: simulation of ELMs, Nucl. Fusion 47 (2007) 659.
[5] A. Cathey, et al., MHD simulations of small ELMs at low triangularity in ASDEX upgrade, Plasma Phys. Control. Fusion 64 (2022) 054011.
[6] J.J. Dominguez Palacios, et al., 2022. (submitted).
[7] T. Eich, et al., ELM divertor peak energy fluence scaling to ITER with data from JET, MAST and ASDEX upgrade, Nucl. Mater. Energy 12 (2017) 84.
[8] G. Federici, et al., Overview of the DEMO staged design approach in Europe, Nucl. Fusion 59 (2019) 066013.
[9] M. Siccinio, et al., DEMO physics challenges beyond ITER, Fusion Eng. Des. 156 (2020) 111603.
[10] M. Maviglia, et al., Impact of plasma-wall interaction and exhaust on the EU-DEMO design, Nucl. Mater. Energy 26 (2021) 100897.
[11] M. Siccinio, et al., Development of the plasma scenario for EU-DEMO: Status and plans, Fusion Eng. Des. 176 (2022) 113047.
[12] J.A. Goetz, et al., High confinement dissipative divertor operation on alcator C-mod, Phys. Plasmas 6 (1999) 1899.
[13] A. Kallenbach, et al., Partial detachment of high power discharges in ASDEX upgrade, Nucl. Fusion 55 (2015) 053026.
[14] A.W. Leonard, et al., Plasma detachment in divertor tokamaks, Plasma Phys. Control. Fusion 60 (2018) 044001.
[15] R.A. Pitts, et al., Physics basis for the first ITER tungsten divertor, Nucl. Mater. Energy 20 (2019) 100696.
[16] N. Oyama, et al., Pedestal conditions for small ELM regimes in tokamaks, Plasma Phys. Control. Fusion 48 (2006) A171.
[17] K. Kamiya, et al., Edge localized modes: recent experimental findings and related issues, Plasma Phys. Control. Fusion 49 (2007) S43.
[18] T.E. Evans, ELM mitigation techniques, J. Nucl. Mater. 438 (2013) S11.
[19] P. Lang, et al., ELM control strategies and tools: status and potential for ITER, Nucl. Fusion 53 (2013) 043004.
[20] R. Maingi, Enhanced confinement scenarios without large edge localized modes in tokamaks: control, performance, and extrapolability issues for ITER, Nucl. Fusion 54 (2014) 114016.
[21] E. Viezzer, et al., Access and sustainment of naturally ELM-free and small-ELM regimes, Nucl. Fusion 58 (2018) 115002.
[22] T. Eich, et al., Scaling of the tokamak near the scrape-off layer H-mode power width and implications for ITER, Nucl. Fusion 53 (2013) 093031.
[23] F. Ryter, et al., H-mode power threshold and transition in ASDEX upgrade, Plasma Phys. Control. Fusion 40 (1998) 725.
[24] M. Greenwald, et al., Transport phenomena in alcator C-mod H-modes, Plasma Phys. Control. Fusion 40 (1998) 789.
[25] D. Whyte, et al., I-mode: an H-mode energy confinement regime with L-mode particle transport in alcator C-mod, Nucl. Fusion 50 (2010) 105005.
[26] K.H. Burrell, et al., Quiescent double barrier high-confinement mode plasmas in the DIII-D tokamak, Phys. Plasmas 8 (2001) 2153.
[27] C.M. Greenfield, et al., Quiescent double barrier regime in the DIII-D tokamak, Phys. Rev. Lett. 86 (2001) 4544.
[28] Y. Takase, et al., Radiofrequency-heated enhanced confinement modes in the alcator C-mod tokamak, Phys. Plasmas 4 (1997) 1647.
[29] M. Greenwald, et al., Characterization of enhanced dalpha high-confinement modes in alcator C-mod, Phys. Plasmas 6 (1999) 1943.
[30] J. Stober, et al., Type II ELMy H modes on ASDEX upgrade with good confinement at high density, Nucl. Fusion 41 (2001) 1123.
[31] G. Saibene, et al., Characterization of small ELM experiments in highly shaped single null and quasi-double-null plasmas in JET, Nucl. Fusion 45 (2005) 297.
[32] G.F. Harrer, et al., Parameter dependences of small edge localized modes (ELMs), Nucl. Fusion 58 (2018) 112001.
[33] B. Labit, et al., Dependence on plasma shape and plasma fueling for small edge-localized mode regimes in TCV and ASDEX upgrade, Nucl. Fusion 59 (2019) 086020.
[34] C. Giroud, et al., High performance ITER-baseline discharges in deuterium with nitrogen and neon-seeding in the JET-ilw, in: IAEA Fusion Energy Conference, 2021, pp. EX/P3–9.
[35] M. Bernert, et al., X-point radiation, its control and an ELM suppressed radiating regime at the ASDEX upgrade tokamak, Nucl. Fusion 61 (2021) 024001.
[36] A. Pochelon, et al., Energy confinement and mhd activity in shaped TCV plasmas with localized electron cyclotron heating, Nucl. Fusion 39 (1999) 1807.
[37] J.M. Moret, et al., Influence of plasma shape on transport in the TCV tokamak, Phys. Rev. Lett. 79 (1997) 2057.
[38] A. Grosman, et al., H-mode barrier control with external magnetic perturbations, J. Nucl. Mater. 313 (2003) 1314.

[39] T.E. Evans, et al., Edge stability and transport control with resonant magnetic perturbations in collisionless tokamak plasmas, Nat. Phys. 2 (2006) 419.
[40] W. Suttrop, et al., First observation of edge localized modes mitigation with resonant and nonresonant magnetic perturbations in ASDEX upgrade, Phys. Rev. Lett. 106 (2011) 225004.
[41] P.T. Lang, et al., ELM pace making and mitigation by pellet injection in ASDEX upgrade, Nucl. Fusion 44 (2004) 665.
[42] L.R. Baylor, et al., Pellet fuelling, ELM pacing and disruption mitigation technology development for ITER, Nucl. Fusion 49 (2009) 085013.
[43] S.K. Combs, et al., Alternative techniques for injecting massive quantities of gas for plasma-disruption mitigation, IEEE Trans. Plasma Sci. 38 (2010) 400.
[44] E. de la Luna, et al., Understanding the physics of ELM pacing via vertical kicks in JET in view of ITER, Nucl. Fusion 56 (2016) 026001.
[45] J.X. Rossel, et al., Nucl. Fusion 52 (2012) 032004.
[46] N. Oyama, et al., J. Phys.: Conf. Ser. 123 (2008) 012002.
[47] M.N.A. Beurskens, et al., Pedestal and ELM response to impurity seeding in JET advanced scenario plasmas, Nucl. Fusion 48 (2008) 095004.
[48] M. Bernert, et al., Power exhaust by SOL and pedestal radiation at ASDEX upgrade and JET, Nucl. Mat. Energy 12 (2017) 111.
[49] A. Loarte, et al., Characteristics and scaling of energy and particle losses during type I ELMs in JET H-modes, Plasma Phys. Control. Fusion 44 (2002) 1815.
[50] R.M. McDermott, et al., Edge radial electric field structure and its connections to H-mode confinement in alcator C-mod plasmas, Phys. Plasmas 16 (2009) 056103.
[51] P. Manz, et al., Physical mechanism behind and access to the I-mode confinement regime in tokamaks, Nucl. Fusion 60 (2020) 096011.
[52] P. Manz, et al., Gyrofluid simulation of an I-mode pedestal relaxation event, Phys. Plasmas 20 (2021) 102502.
[53] Y. Lang, et al., Simulation study of particle transport by weakly coherent mode in the alcator C-mod tokamak, Nucl. Fusion 62 (2022) 086018.
[54] J.R. Walk, et al., The I-mode confinement regime at ASDEX upgrade: global properties and characterization of strongly intermittent density fluctuations, Phys. Plasmas 21 (2014) 056103.
[55] T. Happel, et al., The I-mode confinement regime at ASDEX upgrade: global properties and characterization of strongly intermittent density fluctuations, Plasma Phys. Control. Fusion 59 (2016) 014004.
[56] T. Happel, et al., Stationarity of I-mode operation and I-mode divertor heat fluxes on the ASDEX upgrade tokamak, Nucl. Mater. Energy 18 (2019) 159.
[57] J. Rice, et al., Core impurity transport in alcator C-mod L-, I- and H-mode plasmas, Nucl. Fusion 55 (2015) 033014.
[58] A.E. Hubbard, et al., Multi-device studies of pedestal physics and confinement in the I-mode regime, Nucl. Fusion 56 (2016) 086003.
[59] F. Ryter, et al., I-mode studies at ASDEX upgrade: L-I and I-H transitions, pedestal and confinement properties, Plasma Phys. Control. Fusion 57 (2017) 016004.
[60] A. Creely, et al., Overview of the SPARC tokamak, J. Plasma Phys. 86 (2020) 865860502.
[61] J. Hughes, et al., Projections of H-mode access and edge pedestal in the SPARC tokamak, J. Plasma Phys. 86 (2020) 865860504.
[62] P. Rodriguez Fernandez, et al., Overview of the SPARC physics basis towards the exploration of burning-plasma regimes in high-field, compact tokamaks, Nucl. Fusion 62 (2022) 042003.
[63] A.E. Hubbard, et al., Edge energy transport barrier and turbulence in the I-mode regime on alcator C-mod, Phys. Plasmas 18 (2011) 056115.
[64] O. Grover, et al., private communication.
[65] A. Marinoni, et al., Characterization of density fluctuations during the search for an I-mode regime on the DIII-D tokamak, Nucl. Fusion 55 (2015) 093019.
[66] X. Feng, et al., I-mode investigation on the experimental advanced superconducting tokamak, Nucl. Fusion 59 (2019) 096025.
[67] Y.J. Liu, et al., Power threshold and confinement of the I-mode in the EAST tokamak, Nucl. Fusion 60 (2020) 082003.
[68] S.-W. Yoon, KSTAR overview based on the results of the 2021 campaign, in: APS-DPP Conference on Plasma Physics, Pittsburgh, USA, 2021, p. PO09.00001.
[69] T. Happel, et al., Plasma Phys. Control. Fusion 59 (2017) 014004.
[70] D. Silvagni, et al., I-mode pedestal relaxation events at ASDEX upgrade, Nucl. Fusion 60 (2020) 126028.
[71] D. Silvagni, et al., I-mode pedestal relaxation events in the alcator C-mod and ASDEX upgrade tokamaks, Nucl. Fusion 62 (2022) 036004.
[72] N. Bonanomi, et al., I-mode in non-deuterium plasmas in ASDEX upgrade, Nucl. Fusion 61 (2021) 054001.
[73] X.M. Zhong, et al., Characterization of pedestal burst instabilities during I-mode to H-mode transition in the EAST tokamak, Nucl. Fusion 62 (2022) 066046.
[74] M. Reinke, et al., Radiative heat exhaust in alcator C-mod I-mode plasmas, Nucl. Fusion 59 (2019) 046018.
[75] T. Happel, et al., Approaching detachment in I-mode-response of core confinement and the edge pedestal in the ASDEX upgrade tokamak, Nucl. Fusion 61 (2021) 036026.
[76] W. Suttrop, et al., Plasma Phys. Control. Fusion 45 (2003) 1399.
[77] E.R. Solano, et al., Phys. Rev. Lett. 104 (2010) 185003.
[78] Y. Sakamoto, et al., Plasma Phys. Control. Fusion 46 (2004) A299.
[79] K. Kamiya, et al., Unveiling the structure and dynamics of peeling mode in quiescent high-confinement tokamak plasmas, Commun. Phys. 4 (2021) 141.
[80] K.H. Burrell, et al., Discovery of stationary operation of quiescent H-mode plasmas with net-zero neutral beam injection torque and high energy confinement on DIII-D, Phys. Plasmas 23 (2016) 056103.
[81] X. Chen, et al., Nucl. Fusion 57 (2017) 022007.
[82] X. Chen, et al., Nucl. Fusion 57 (2017) 086008.
[83] T.M. Wilks, et al., Nucl. Fusion 58 (2018) 112002.
[84] K.H. Burrell, et al., Quiescent H-mode plasmas with strong edge rotation in the cocurrent direction, Phys. Rev. Lett. 102 (2009) 155003.
[85] X. Chen, et al., Expanding the parameter space of the wide-pedestal QH-mode towards ITER conditions, Nucl. Fusion 60 (2020) 092006.
[86] T.M. Wilks, et al., Impact of shape on pedestal characteristics in the wide pedestal quiescent H-mode in the DIII-D tokamak, Nucl. Fusion 61 (2021) 036032.
[87] K.H. Burrell, et al., Creation and sustainment of wide pedestal quiescent H-mode with zero net neutral beam torque, Nucl. Fusion 60 (2020) 092006.
[88] D. Ernst, et al., IAEA fusion energy conference, 2018.
[89] A. Garofalo, et al., Phys. Plasmas 22 (2015) 056116.
[90] D. Ernst, et al., Real-time wall conditioning experiments in the wide pedestal QH-mode regime, in: APS Division of Plasma Physics Meeting, 2021, p. UP11.119.
[91] D. Ernst, et al., Nucl. Fusion (2022) (in preparation).
[92] K.H. Burrell, et al., Advances in understanding quiescent H-mode plasmas in DIII-D, Phys. Plasmas 12 (2005) 056121.
[93] B. Grierson, et al., Impurity confinement and transport in high confinement regimes without edge localized modes on DIII-D, Phys. Plasmas 22 (2015) 055901.
[94] W. Suttrop, et al., Studies of the 'quiescent H-mode' regime in ASDEX upgrade and JET, Nucl. Fusion 45 (2005) 721.
[95] K.H. Burrell, et al., Quiescent H-mode plasmas in the DIII-D tokamak, Plasma Phys. Control. Fusion 44 (2002) A253.
[96] C. Paz-Soldan, et al., Plasma performance and operational space without ELMs in DIII-D, Plasma Phys. Control. Fusion 63 (2021) 083001.
[97] E. Viezzer, et al., Progress towards a quiescent, high confinement regime for the all-metal ASDEX upgrade tokamak, in: EPS Conference on Plasma Physics, 2021.
[98] E. Viezzer, et al., Nucl. Fusion (2022) (in Preparation).
[99] J. Hughes, et al., Access to pedestal pressure relevant to burning plasmas on the high magnetic field tokamak alcator C-mod, Nucl. Fusion 58 (2018) 112003.
[100] E.R. Solano, et al., APS conference division plasma physics, 2022.
[101] J. Qian, et al., Development of quiescent H-mode scenario with ITER like tungsten divertor in EAST, in: IAEA Fusion Energy Conference, 2021.
[102] P. Mossessian, et al., Edge dimensionless identity experiment on DIII-D and alcator C-mod, Phys. Plasmas 10 (2003) 689.
[103] P.J. Sun, et al., Experimental study of quasi-coherent mode using EAST tangential CO2 laser collective scattering diagnostic in far-forward mode, Phys. Plasmas 26 (2019) 012304.
[104] L. Gil, et al., Stationary ELM-free H-mode in ASDEX upgrade, Nucl. Fusion 60 (2020) 054003.
[105] M. Greenwald, et al., Confinement and transport research in alcator C-mod, Fusion Sci. Technol. 51 (2007) 266.
[106] M. Griener, et al., Continuous observation of filaments from the confined region to the far scrape-off layer, Nucl. Mater. Energy 25 (2020) 100854.
[107] P. Mossessian, et al., H-mode pedestal characteristics and MHD stability of the edge plasma in alcator C-mod, Plasma Phys. Control. Fusion 44 (2002) 423.
[108] L. Gil, et al., 2022. (in Preparation).
[109] T. Puetterich, et al., Nucl. Fusion (2022) (in Preparation).
[110] E.A. Tolman, et al., Influence of high magnetic field on access to stationary H-modes and pedestal characteristics in alcator C-mod, Nucl. Fusion 58 (2018) 046004.
[111] A. Loarte, et al., High confinement/high radiated power H-mode experiments in alcator C-mod and consequences for international thermonuclear experimental reactor (ITER) q=10 operation, Phys. Plasmas 18 (2011) 056105.
[112] J.W. Hughes, et al., Power requirements for superior H-mode confinement on alcator C-mod: experiments in support of ITER, Phys. Plasmas 51 (2011) 083007.
[113] A. Kallenbach, et al., Developments towards an ELM-free pedestal radiative cooling scenario using noble gas seeding in ASDEX upgrade, Nucl. Fusion 61 (2021) 016002.
[114] A. Kallenbach, et al., Development towards an ELM-free DEMO pedestal radiative cooling scenario in ASDEX upgrade, in: IAEA Fusion Energy Conference, 2021, p. EX/2.
[115] K. Stimmel, et al., Gyrokinetic analysis of an argon-seeded EDA H-mode in ASDEX upgrade, Phys. Plasmas 88 (2022) 905880315.
[116] T. Ozeki, et al., Plasma shaping, edge ballooning stability and ELM behaviour in DIII-D, Nucl. Fusion 30 (1990) 1425.
[117] E. Wolfrum, et al., Characterization of edge profiles and fluctuations in discharges with type-II and nitrogen-mitigated edge localized modes in ASDEX upgrade, Plasma Phys. Control. Fusion 53 (2011) 085026.

[118] A. Kirk, et al., Comparison of small edge-localized modes on MAST and ASDEX upgrade, Plasma Phys. Control. Fusion 53 (2011) 095008.
[119] R. Maingi, et al., Enhanced confinement scenarios without large edge localized modes in tokamaks: control, performance, and extrapolability issues for ITER, Plasma Phys. Control. Fusion 13 (2000) 092510.
[120] Y. Kamada, et al., Plasma Phys. Control. Fusion 42 (2000) A247.
[121] G.S. Xu, et al., Phys. Rev. Lett. 122 (2019) 255001.
[122] Q.Q. Yang, et al., Stationary high-performance grassy ELM regime in EAST, Nucl. Fusion 60 (2020) 076012.
[123] G. Xu, et al., Nucl. Fusion 60 (2020) 086001.
[124] J. Garcia, et al., New H-mode regimes with small ELMs and high thermal confinement in the joint European torus, Phys. Plasmas 29 (2022) 032505.
[125] E. de la Luna, et al., Exploring the physics of a high performance H-mode with small ELMs and zero gas puffing in JET-ILW, in: IAEA Fusion Energy Conference, 2021, pp. EX/3–2.
[126] G.F. Harrer, et al., Quasicontinuous exhaust scenario for a fusion reactor: The renaissance of small edge localized modes, Phys. Rev. Lett. 129 (2022) 165001.
[127] M. Faitsch, et al., Broadening of the power fall-off length in a high density, high confinement H-mode regime in ASDEX upgrade, Nucl. Mater. Energy 26 (2021) 100890.
[128] L. Radovanovic, et al., Developing a physics understanding of the quasi-continuous exhaust regime: pedestal profile and ballooning stability analysis, Nucl. Fusion 62 (2022) 086004.
[129] M. Faitsch, et al., High density, high confinement, power exhaust compatible H-mode regime in TCV and ASDEX upgrade, in: IAEA Fusion Energy Conference, 2021, p. P4/970.
[130] M.G. Dunne, et al., The role of the density profile in the ASDEX upgrade pedestal structure, Plasma Phys. Control. Fusion 59 (2017) 014017.
[131] C. Giroud, et al., High performance ne-seeded baseline scenario in JET-ILW in support of ITER, in: EPS Conference on Plasma Physics, 2022.
[132] C. Giroud, et al., IAEA fusion energy conference, 2014.
[133] J. Mailloux, et al., Overview of JET results for optimising ITER operation, Nucl. Fusion 62 (2022) 042026.
[134] F. Reimold, et al., Divertor studies in nitrogen induced completely detached H-modes in full tungsten ASDEX upgrade, Nucl. Fusion 15 (2015) 033004.
[135] S. Gloeggler, et al., Characterisation of highly radiating neon seeded plasmas in JET-ILW, Nucl. Fusion 59 (2019) 126031.
[136] U. Stroth, et al., Model for access and stability of the X-point radiator and the threshold for marfes in tokamak plasmas, Nucl. Fusion 62 (2022) 076008.
[137] S.Y. Medvedev, et al., Beta limits and edge stability for negative triangularity plasmas in the TCV tokamak, 35th EPS Conference on Plasma Physics 32 (2008) P1.072.
[138] A. Pochelon, et al., Recent TCV results - innovative plasma shaping to improve plasma properties and insight, Plasma and Fusion Research: Overview Articles 7 (2012) 2502148.
[139] M. Kikuchi, et al., L-mode-edge negative triangularity tokamak reactor, Nucl. Fusion 59 (2019) 056017.
[140] A. Marinoni, et al., Diverted negative triangularity plasmas on DIII-D: the benefit of high confinement without the liability of an edge pedestal, Nucl. Fusion 61 (2021) 116010.
[141] Y. Camenen, et al., Impact of plasma triangularity and collisionality on electron heat transport in TCV L-mode plasmas, Nucl. Fusion 47 (2007) 510.
[142] M. Fontana, et al., The effect of triangularity on fluctuations in a tokamak plasma, Nucl. Fusion 58 (2018) 024002.
[143] M. Fontana, et al., Effects of collisionality and Te/Ti on fluctuations in positive and negative triangularity tokamak plasmas, Nucl. Fusion 60 (2020) 016006.
[144] S. Coda, et al., Enhanced confinement in diverted negative-triangularity L-mode plasmas in TCV, Plasma Phys. Control. Fusion 64 (2022) 014004.
[145] M.E. Austin, et al., Achievement of reactor-relevant performance in negative triangularity shape in the DIII-D tokamak, Phys. Rev. Lett. 122 (2019) 115001.
[146] F. Sciortino, et al., Investigation of impurity transport in DIII-D diverted negative triangularity plasmas, Plasma Phys. Control. Fusion 64 (2022) 124002.
[147] F. Bagnato, et al., EPS conference on plasma physics, 2021.
[148] T. Happel, et al., APS conference division plasma physics, 2020.
[149] T. Happel, et al., Overview of initial negative triangularity plasma studies on the ASDEX upgrade tokamak, Nucl. Fusion 63 (2023) 016002, (in press).
[150] A. Merle, et al., Pedestal properties of H-modes with negative triangularity using the EPED-CH model, Plasma Phys. Control. Fusion 59 (2017) 104001.
[151] S. Saarelma, et al., Ballooning instability preventing the H-mode access in plasmas with negative triangularity shape on the DIII–D tokamak, Plasma Phys. Control. Fusion 63 (2021) 105006.
[152] A.O. Nelson, et al., Prospects for H-mode inhibition in negative triangularity tokamak reactor plasmas, Nucl. Fusion 62 (2022) 096020.
[153] M. Faitsch, et al., Dependence of the L-mode scrape-off layer power fall-off length on the upper triangularity in TCV, Plasma Phys. Control. Fusion 60 (2018) 045010.
[154] K. Ikeda, et al., Progress in the ITER physics basis, Nucl. Fusion 6 (2007) E01.
[155] C. Angioni, et al., Impurity transport in tokamak plasmas, theory, modelling and comparison with experiment, Plasma Phys. Control. Fusion 63 (2001) 073001.
[156] S.Y. Medvedev, et al., The negative triangularity tokamak: stability limits and prospects as a fusion energy system, Nucl. Fusion 55 (2015) 063013.